

RESEARCH ARTICLE

10.1029/2019JE005988

Key Points:

- Computation of the viscous dissipation in Enceladus's ocean due to tides and libration
- Libration-induced dissipation generates several orders of magnitude more heat than tidal dissipation
- Inertial mode resonances are related with the excitation of weakly dampened eigenmodes

Correspondence to:

J. Requier,
jeremy.requier@observatory.be

Citation:

Requier, J., Trinh, A., Triana, S. A., & Dehant, V. (2019). Internal energy dissipation in Enceladus's subsurface ocean from tides and libration and the role of inertial waves. *Journal of Geophysical Research: Planets*, 124. <https://doi.org/10.1029/2019JE005988>

Received 4 APR 2019

Accepted 24 JUL 2019

Accepted article online 31 JUL 2019

Internal Energy Dissipation in Enceladus's Subsurface Ocean From Tides and Libration and the Role of Inertial Waves

J. Requier¹ , A. Trinh¹, S. A. Triana¹ , and V. Dehant¹

¹Royal Observatory of Belgium, Uccle, Belgium

Abstract Enceladus is characterized by a south polar hot spot associated with a large outflow of heat, the source of which remains unclear. We compute the heat generated via viscous dissipation resulting from tidal and (longitudinal) libration forcing in the moon's subsurface ocean using the linearized Navier-Stokes equation in a three-dimensional spherical model. We conclude that libration is the dominant cause of dissipation at the linear order, providing up to ~0.001 GW of heat to the ocean, which remains insufficient to explain the ~10 GW observed by Cassini. We also illustrate how resonances with inertial modes can significantly augment the dissipation. Our work is an extension to Rovira-Navarro et al. (2019, <https://doi.org/10.1016/j.icarus.2018.11.010>) to include the effects of libration and the presence of the icy crust. The model developed here is readily applicable to the study of other moons with a subsurface ocean and planets with a liquid core.

Plain Language Summary From the massive amount of information collected by Cassini, Saturn's moon Enceladus currently appears as one of the most habitable moons in the Solar System. Various observations have pointed out the existence of a very active global liquid subsurface water ocean and geysers have also been observed at the moon's south pole indicating a significant amount of geothermal activity. Tidal dissipation is the most likely candidate to explain the heat flux observed at the moon's surface. There is, however, a major discrepancy between the magnitude of the observed heat flux and current estimations from mathematical models. In this work, we focus on the viscous dissipation taking place in the ocean with a special emphasis put on the role played by libration. We have found that libration is the dominant cause of dissipation in the ocean but that it is insufficient to explain the observed heat flux. We also demonstrate how inertial waves (which are waves supported by the Coriolis force) can significantly increase the amount of dissipation via resonance although not sufficiently to challenge the predominance of libration.

1. Introduction

From the massive amount of information collected by Cassini, Saturn's moon Enceladus currently appears as one of the most habitable moons in the Solar System. The presence of a subsurface reservoir of liquid water was inferred soon after the first few flybys (Porco et al., 2006). Measurements of the gravity field deduced from subsequent flybys helped establish the large spatial extent of this reservoir (Iess et al., 2014), and libration observations finally provided the definitive evidence for a global-scale ocean rather than a regional sea (Thomas et al., 2016).

Tidal dissipation is the most likely source of power for the observed geological activity (Nimmo et al., 2018). Current models, however, have so far been unable to account for the observed ~10 GW of endogenic heat flow emanating from the south polar region (Howett et al., 2011; Spencer et al., 2006) without invoking the presence of a highly porous ("fluffy") solid inner core (Choblet et al., 2017; Roberts, 2015) or a convecting icy crust (Běhouňková et al., 2010, 2017). As suggested by Barr and McKinnon (2007), this latter hypothesis appears unlikely in view of the relatively small thickness of the crust (~20 km) deduced from geodetic observations (Beuthe et al., 2016; Čadež et al., 2016).

If dissipation is not concentrated in the core or in the shell, one possibility is that it takes place predominantly in the ocean. Most of the current models focusing specifically on the ocean layer rely on the solution of the Laplace Tidal Equations (LTE) whereby the fluid is modeled as a two-dimensional thin layer

(Beuthe et al., 2016; Hay & Matsuyama, 2017; Matsuyama et al., 2018; Tyler, 2009, 2014). However, gravity and topography data suggest that the average thickness of the ocean is not negligible compared to the size of the moon, ~ 38 km if the crustal topography is isostatically supported, which is also consistent with the thin crust inferred from libration (Beuthe et al., 2016; Hemingway & Mittal, 2019). Such a thick ocean challenges the validity of the conclusions drawn from the 2-D models.

Additionally, the action of the Coriolis force on planetary oceans is known to support the existence of inertial waves within their volume, which are oscillatory motions supported by the Coriolis force (Poincaré, 1885), and Morize et al. (2010) have shown how these can be excited through tidal deformation in their laboratory experiment. The role that the inertial waves play in planetary and astrophysical settings is still, however, far from clear. When viscosity is taken into account, the flow associated with these waves develops regions of intense shear within the fluid volume (Greenspan, 1968). These *internal shear layers* can significantly increase the total amount of dissipation in the ocean (Ogilvie, 2009). This can be understood by looking at the formula giving the total heat generated by viscosity for a flow of velocity field \mathbf{v} (see, e.g., Landau & Lifshitz, 1987):

$$D_{\text{visc}} = 2 \text{Ek} \int_V \widehat{\nabla \mathbf{v}} : \widehat{\nabla \mathbf{v}}, \quad (1)$$

with $\widehat{\nabla \mathbf{v}} \equiv \frac{1}{2}(\nabla \mathbf{v} + \nabla \mathbf{v}^T)$ and where Ek denotes the Ekman number (see equation (21)), which is typically very small in planetary applications ($\text{Ek} \sim 10^{-13}$ for Enceladus). In order to significantly contribute to the total dissipation, the gradient of velocity within the ocean volume in general and in the internal shear layers in particular must be sufficiently strong to compensate the smallness of the Ekman number. A study of the problem has recently been conducted by Rovira-Navarro et al. (2019) who concluded to the irrelevance of inertial waves in the energy budget. We reproduce their results in the present paper and extend them to include the contribution from libration which corresponds to a forcing with a much larger amplitude. Our model also has the advantage to take the presence of the icy crust into account. As the obliquity of Enceladus is very small (Baland et al., 2016), we focus our attention on the effects of eccentricity tides, which are likely to dominate over obliquity tides in the ocean layer (Chen & Nimmo, 2011; Tyler, 2014), even though, recent work by Hay and Matsuyama (2019) has shown that nonlinear effects can alter this picture at least within the simplified model based on the LTE.

It is worth mentioning that Tyler (2009) showed how the obliquity tides can excite large amplitude Rossby waves leading to high dissipation thus solving the heat budget paradox, at least in the thin ocean limit. This scenario, however, requires a relatively large value of the obliquity angle ($\gtrsim 0.1^\circ$). Although the obliquity of Enceladus has not been measured, the theoretical estimates predict a much smaller value of the order of $\sim 0.0001^\circ$ (Baland et al., 2016), and so eccentricity tides are likely to dominate in the ocean layer (Chen & Nimmo, 2011; Tyler, 2014). Furthermore, as far as inertial waves are concerned, one can see from the results of Rovira-Navarro et al. (2019) that the obliquity angle needs to be higher than 0.1° simply to match the dissipation from eccentricity tides (this can be understood from the fig. 5b of Rovira-Navarro et al., 2019, and the fact that the dissipation scales with the square of the forcing amplitude). For this reason, we focus solely on the eccentricity tides and disregard the tides of obliquity in the present paper. It is however still possible that nonlinear effects alter this picture, as was shown recently by Hay and Matsuyama (2019), at least based on their model using the LTE.

The approach presented here is complementary to the studies based on the resolution of the LTE. The latter are unable to model the appearance of internal shear layers inside the ocean and the dissipation that these entails. On the other hand, our method is limited to the modeling of the fluid dynamics inside the ocean and is, therefore, not suited to model other processes such as surface gravity waves for which the LTE are more appropriate.

The principal focus of our study is to provide an estimate of the contribution of the inertial modes and associated internal shear layers to the total viscous dissipation in Enceladus's subsurface ocean. We do so by modeling the moon as a three-layer spherical body, each layer with its own homogeneous density. This simple model allows us to estimate the order of magnitude of the heat produced by tidally forced inertial modes.

The present paper is structured as follows. In section 2, we present our model including the details on the equilibrium state and the equations of motion and how these are used to compute the response to tidal

Table 1
List of Physical Parameters

Name	Symbol	Core	Ocean	Crust
Outer radius (km)	R	192	[192–252]	252
Mass Density (kg/m ³)	ρ	[2,483–2,357] ^a	1,020	920
Shear modulus (GPa)	μ	40	0	3.5

^aThe density of the core is adjusted to conserve the total mass ($M = 1.080 \times 10^{20}$ kg).

and libration forcing. We also explain how we use the resulting displacement to force the Navier-Stokes equation describing the flow velocity inside the ocean and the way to compute the heat generated via viscous dissipation. The results are presented in section 3 and discussed in section 4. In this last section, we also provide a new interpretation of our results in terms of resonance with inertial waves and conclude with perspectives about the possible continuations of the present work.

2. Method

In a recent paper (Triana et al., 2019), we explained the difficulties of solving the equations of hydrodynamics at low Ekman number for geometries that are too far from the simple spherical symmetry. This is because the flow develops a very thin *Ekman boundary layer* that needs to be resolved numerically. To avoid this difficulty, we proceed in two steps. First, we compute the deformation at the ocean's boundary of a nonrotating spherical model (section 2.1), and then we compute the flow resulting from this deformation of the spherical shell when rotation taken into account (section 2.2). In the second step of our model, the motion of the fluid at the top (and bottom) of the ocean is equal to the displacement computed in the first step. This amounts to neglect the feedback of the inertial waves at the ocean's boundaries. However, Rovira-Navarro et al. (2019) have shown that the pressure due to inertial waves at the ocean's surface does not exceed a few pascals, which makes this assumption reasonable.

2.1. Deformation

2.1.1. Equilibrium State

We model the moon as a set of three homogeneous concentric spherical shells, and we assume that each layer is incompressible. Table 1 gives the set of parameters used in the present paper. We set the size of the core to the central value 192 km obtained by Beuthe et al. (2016) with the reference data sets and consider a range of interior models with variable ocean thickness.

In what follows, we use the symbol η to represent the aspect ratio of the spherical shell defined as

$$\eta = \frac{R_{\text{core}}}{R_{\text{ocean}}}. \quad (2)$$

2.1.2. Equations of Deformation

The equation governing the oscillation around the equilibrium state is the Poisson equation and the conservation of momentum. Assuming incompressibility, these read (Dahlen & Tromp, 1998)

$$\nabla^2 \delta\phi = 0, \quad (3)$$

$$-\omega^2 \rho \mathbf{s} = \nabla \cdot \Delta \boldsymbol{\sigma} - \nabla(\rho \mathbf{s} \cdot \nabla \phi_0) - \rho \nabla \delta\phi, \quad (4)$$

where ϕ_0 is the equilibrium gravity potential, $\delta\phi$ denotes the (Eulerian) increments of gravity (i.e., self-gravitational + tidal) potential, \mathbf{s} is the displacement vector field, and $\Delta \boldsymbol{\sigma}$ denotes the (Lagrangian) increment of Cauchy stress. The latter can be expressed in terms of the displacement and (Lagrangian) increment of pressure:

$$\Delta \boldsymbol{\sigma} \equiv -p\mathbf{g} + \mu (\nabla \mathbf{s} + \nabla \mathbf{s}^T), \quad (5)$$

where \mathbf{g} is the metric tensor. μ denotes the shear modulus, which is assumed to be constant in each layer, its values are listed in Table 1, as well as those for the density, ρ .

The gravity potential, displacement vector, and stress tensor must satisfy the following conditions at each undeformed spherical boundary Dahlen and Tromp (1998):

$$[\delta\phi]_{\pm}^+ = 0, \quad (6)$$

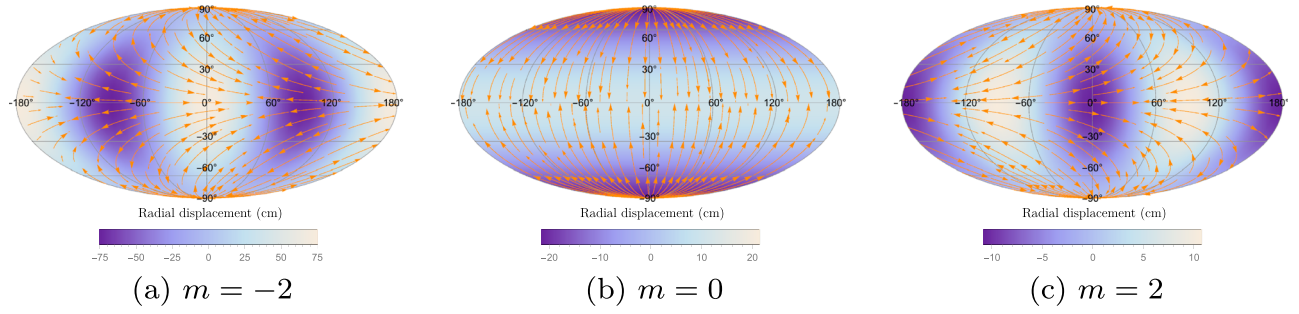


Figure 1. Eccentricity tides — Deformation patterns at the top of Enceladus' ocean for the three components of the tidal potential (aspect ratio $\eta = 0.838$). The arrows indicate the tangential displacement and are not to scale.

$$[\hat{\mathbf{n}} \cdot (\nabla \delta\phi + 4\pi G\rho\mathbf{s})]_{-}^{+} = 0, \quad (7)$$

$$[\hat{\mathbf{n}} \cdot \Delta\sigma]_{-}^{+} = 0, \quad (8)$$

where $\hat{\mathbf{n}}$ is the normal vector and the notation $[\cdot]_{-}^{+}$ denotes the difference between the values of the enclosed quantity on both sides of the boundary. The last constraint is that the normal component of the displacement be continuous across each internal boundary:

$$[\hat{\mathbf{n}} \cdot \mathbf{s}]_{-}^{+} = 0. \quad (9)$$

The above does not hold at the free outermost boundary.

2.1.3. Tidal Deformation

Enceladus gets deformed under the effect of tides caused by its slightly eccentric orbit around Saturn (eccentricity tides). The corresponding (Eulerian) increment of gravity potential can be decomposed in terms of spherical harmonics:

$$\delta\phi = \sum_{\ell=0}^{\infty} \sum_{m=-\ell}^{\ell} \delta\phi_{\ell,m} Y_{\ell}^m(\theta, \lambda) e^{i\omega t} + c.c., \quad (10)$$

where θ and λ denote the colatitude and (east) longitude, respectively. The only nonzero components of the tidal potential are

$$\delta\phi_{2,-2}^{\text{tide}} = -\frac{7}{4} \sqrt{\frac{3}{2}} e \omega^2 r^2, \quad (11)$$

$$\delta\phi_{2,0}^{\text{tide}} = \frac{3}{4} e \omega^2 r^2, \quad (12)$$

$$\delta\phi_{2,2}^{\text{tide}} = \frac{1}{4} \sqrt{\frac{3}{2}} e \omega^2 r^2, \quad (13)$$

where $\omega = \frac{2\pi}{1.37} \text{ day}^{-1}$ is the (diurnal) frequency of the forcing and $e = 4.7 \times 10^{-3}$ denotes the orbital eccentricity. We use the following definition of the spherical harmonics, $Y_{\ell}^m(\theta, \lambda)$, and the associated Legendre functions, $P_{\ell}^m(x)$:

$$Y_{\ell}^m(\theta, \lambda) = \sqrt{\frac{(\ell-m)!}{(\ell+m)!}} P_{\ell}^m(\cos \theta) e^{im\lambda}, \quad (14)$$

$$P_{\ell}^m(x) = \frac{(-1)^m}{2^{\ell} \ell!} (1-x^2)^{\frac{m}{2}} \frac{d^{\ell+m}}{dx^{\ell+m}} (x^2-1)^{\ell}. \quad (15)$$

Figure 1 shows the spatial pattern for each tidal component for $\eta = 0.838$ corresponding to a shell thickness of 23 km, the central value predicted by the model of isostasy of Beuthe et al. (2016).

2.1.4. Libration Forcing

Enceladus is not, in reality, spherical. And this fact influences its rotation. In particular, the equilibrium deformation caused by permanent tides induces a periodic motion of longitudinal libration under the perturbing effect of gravitational torques from external sources and the restoring effect of internal pressure and gravitational torques (inertial torques).

In the present paper, we treat the libration motion as a given and compute the resulting dissipation in the fluid layer of our simplified spherical setting. Our model of libration is based on the rigid-shell model of Baland and Van Hoolst (2010); we therefore neglect the limited decrease of libration amplitude introduced by elastic deformation (Van Hoolst et al., 2016). For the present, it is sufficient to observe that the libration of the ocean's flattened boundaries can be represented as a superposition of several oscillations of fictitious spherical boundaries: a toroidal degree-1 oscillation where the librating spherical boundaries tend to viscously drag the ocean and a spheroidal degree-2 oscillation where the librating flattened boundaries tend to push the ocean fluid, as if spherical boundaries underwent radial deformation.

The tangential displacement can be obtained directly from the libration amplitude as a function of η , the aspect ratio of the ocean (see Figure A2 of section A2). It results in what is later referred to as the $m = 0$ component.

The nonaxisymmetric shape of Enceladus also causes a radial displacement at the top and bottom of the ocean, which can be estimated in the following manner. To first order, the radial coordinate of the triaxial boundary can be approximated as

$$r(\theta, \lambda) = R\{1 + \alpha_0 Y_2^0(\theta, \lambda) + \alpha_2[Y_2^2(\theta, \lambda) + Y_2^{-2}(\theta, \lambda)]\}, \quad (16)$$

where R is the mean radius and α_0 and α_2 are real numbers describing the polar and equatorial flattening, which we assume to be hydrostatic. In the frame rotating at constant angular velocity Ω , libration can be accounted for by replacing $\lambda \rightarrow \lambda + \delta(t)$ with $\delta \ll 1$. The first two terms in equation (16) do not depend on the azimuthal angle, λ , and so the velocity of the moving boundary comes out to be

$$\frac{\dot{r}}{R} = 2i\alpha_2\dot{\delta}[Y_2^2(\theta, \lambda) - Y_2^{-2}(\theta, \lambda)]. \quad (17)$$

Now, if we set $\delta(t) = \epsilon \sin(\omega t)$, where ϵ and ω denote the amplitude and the (diurnal) frequency of libration, respectively, we obtain

$$\frac{\dot{r}}{R} = 2\alpha_2\epsilon(i\omega)[Y_2^2(\theta, \lambda) - Y_2^{-2}(\theta, \lambda)]\cos(\omega t). \quad (18)$$

The values of the (hydrostatic) flattening parameter α_2 and the amplitude of libration ϵ both depend on the aspect ratio η . We give simplified expressions of these in section A2. Hereafter, the radial displacement is referred to as the $m = \pm 2$ components.

2.2. Viscous Dissipation

We use the (linearized) Navier-Stokes equation to model the motion of the ocean. In its dimensionless form and in the frame rotating with angular velocity $\Omega \equiv \Omega \hat{\mathbf{z}}$, this reads

$$i\omega \mathbf{v} + 2\hat{\mathbf{z}} \times \mathbf{v} + \nabla p - \text{Ek} \nabla^2 \mathbf{v} = 0, \quad (19)$$

where \mathbf{v} denotes the velocity and p denotes the reduced pressure related to the physical pressure, P , through

$$p \equiv \frac{P}{\rho} - \frac{1}{2}|\hat{\mathbf{z}} \times \mathbf{r}|^2 + \Phi, \quad (20)$$

where Φ is the gravitational potential.

The Ekman number parametrizes the balance between the viscous force and the Coriolis force. We define it as such

$$\text{Ek} \equiv \frac{\nu}{\Omega R_o^2}, \quad (21)$$

where ν denotes the kinematic viscosity (here taken to be that of water: $\nu = 10^{-6} \text{m}^2/\text{s}$) and R_o is the (mean) radius at the top of the ocean. In planetary settings, Ek is typically very small. For Enceladus, its value is of

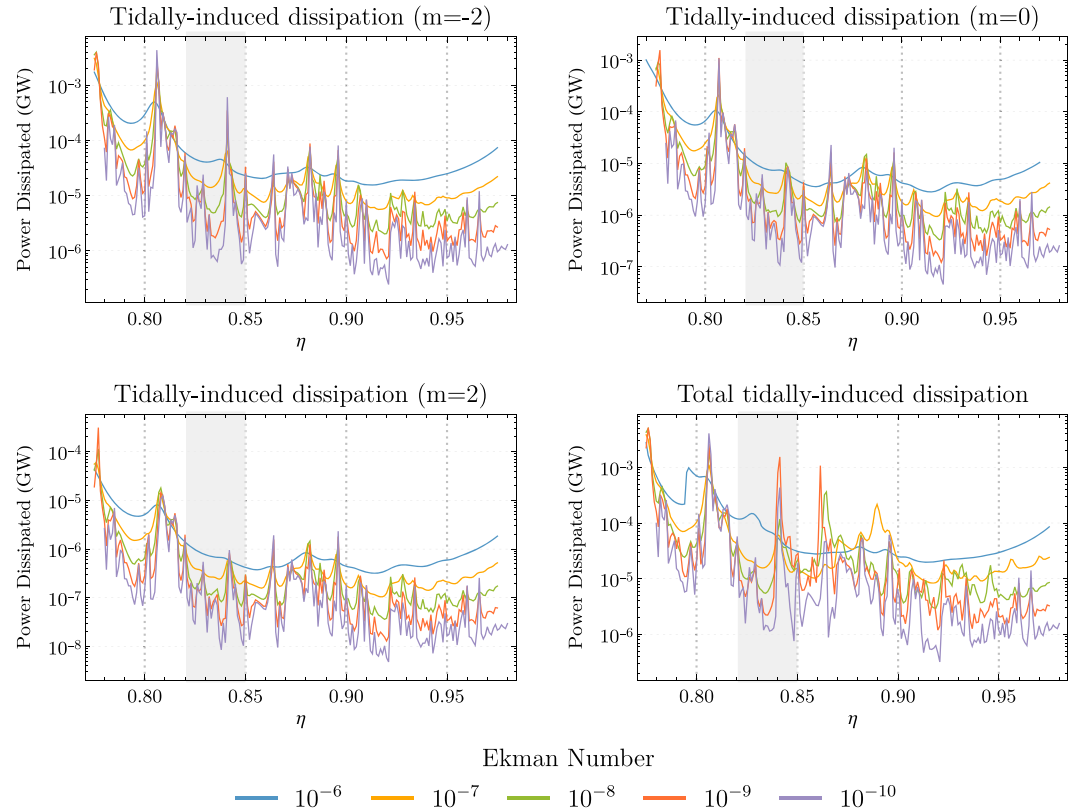


Figure 2. Eccentricity tides — Viscous dissipation in Enceladus's ocean as a function of η , the aspect ratio of the spherical shell, for different values of the Ekman number. The bottom-right plot is the sum of all the others. The shaded area represents the range $0.82 \leq \eta \leq 0.85$ predicted by models of isostasy.

the order $\text{Ek} \sim 3.5 \times 10^{-13}$. There is actually a lot of uncertainty on the precise value of this parameter. Here we are only interested in its order of magnitude.

The motion inside the ocean is forced by the deformation of the boundary caused by tides and libration. We recover the velocity of the moving boundary from the displacement vector \mathbf{s} via

$$\mathbf{v}_{\text{tide/libration}} = i\omega \mathbf{s}_{\text{tide/libration}}. \quad (22)$$

We use the *no-slip* boundary condition, which, in this case, amounts to impose that the velocity is continuous across the boundary (at the top and bottom of the ocean):

$$\mathbf{v} = \mathbf{v}_{\text{tide/libration}}. \quad (23)$$

To first order, it is sufficient to enforce this condition at the boundary of the (spherical) equilibrium figure. Owing to the condition of incompressibility ($\nabla \cdot \mathbf{v} = 0$), we can write the velocity field as (see, e.g., Backus, 1986)

$$\mathbf{v} = \nabla \times \nabla \times (\mathcal{P} \mathbf{r}) + \nabla \times (\mathcal{T} \mathbf{r}), \quad (24)$$

where \mathcal{P} and \mathcal{T} denote the poloidal and toroidal potentials, respectively. These are then decomposed in terms of their spherical harmonics coefficients, $\mathcal{P}_{\ell,m}$ and $\mathcal{T}_{\ell,m}$.

2.3. Numerical Implementation

We solve equations (3) and (4) analytically. The procedure to do so is outlined in section A1. This essentially amounts to compute *Tidal Love Numbers* (Love, 1909). Instead of giving the analytical expression explicitly (which are quite lengthy and impractical), we provide a Pade approximant of tidal response to a unit forcing as a function of η in section A1. The displacement resulting from longitudinal libration is computed analytically using the model of Van Hoolst et al. (2016) and Pade approximants are also given in section A2.

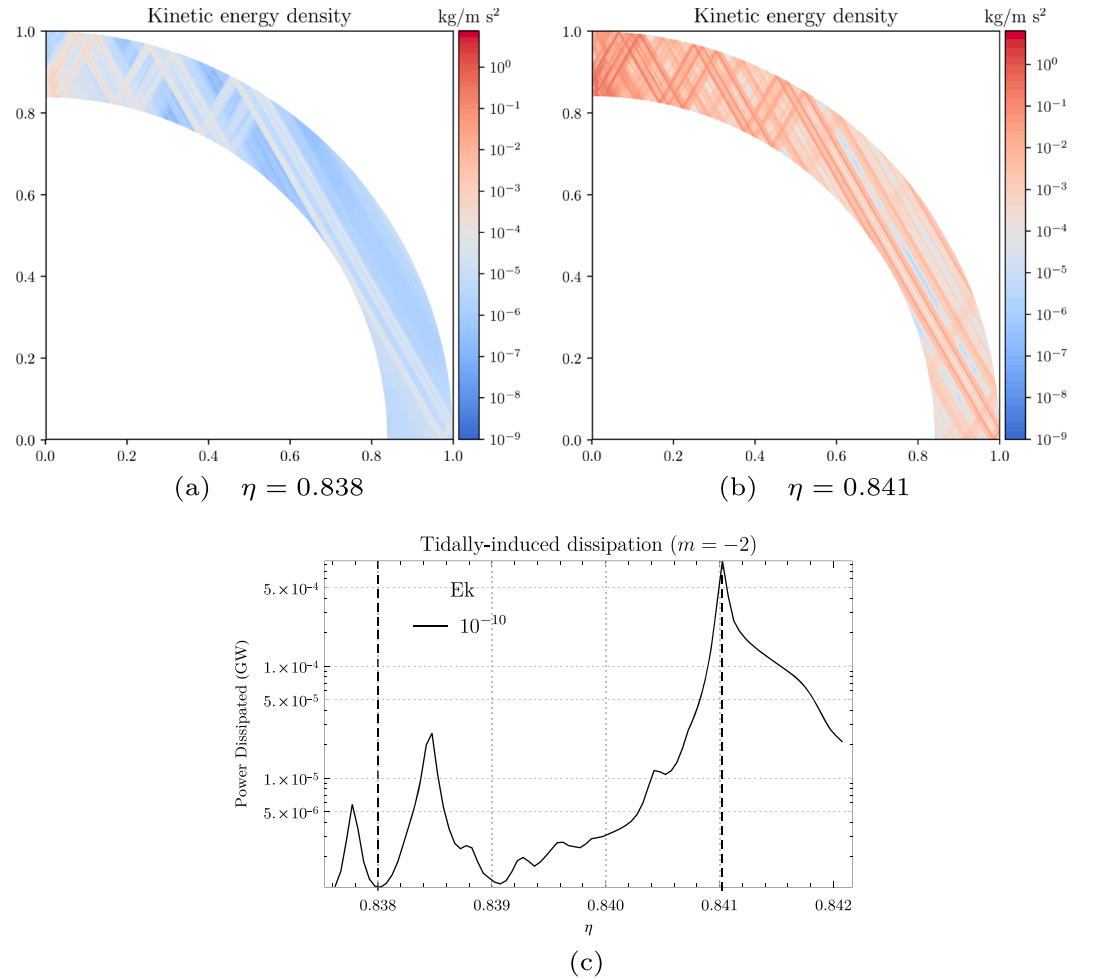


Figure 3. Eccentricity tides — (a) and (b): Density of kinetic energy inside the ocean for two values of the aspect ratio, η , close to its actual value for Enceladus ($m = -2$, $Ek = 10^{-10}$). The associated amounts of dissipation for each case is shown in (c) and differ by 3 orders of magnitude.

Rather than solving equation (19) directly for the flow velocity, v , we use the projections equations (C1) and (C2) presented in Appendix C, there given in terms of their spherical harmonics components. We solve these equations numerically using a dedicated spectral solver described in some details in Rekier et al. (2018) and Triana et al. (2019). The spherical harmonics components $\mathcal{P}_{\ell,m}(r)$ and $\mathcal{T}_{\ell,m}(r)$ are discretized in the radial direction by using a representation in terms of Chebyshev coefficients.

The Ekman number is the main source of difficulties in this kind of study. A small value of Ek demands a large spatial resolution. Thanks to the efficiency of our method and the fact that it is based on an algebraic representation in terms of sparse matrices, we are able to reach values of $Ek \lesssim 10^{-10}$. See Rekier et al. (2018) and Triana et al. (2019) for more details.

We have developed a Python code to solve the Navier-Stokes equation based on the numerical methods presented here. It is open source and publicly available online (<https://bitbucket.org/repepo/tintin>). The formal release of this code will be the subject of a future publication.

3. Results

3.1. Tides

Figure 2 shows the dissipation for $m \in \{-2, 0, 2\}$ and the total dissipation for all these contributions (lower-right panel). There is a general trend toward more dissipation as η decreases. This is because the amplitude of the forcing is bigger in this regime where the icy shell is thinner (see Figure A1). The higher dissipation in this regime follows the same trend as indicated by Matsuyama et al. (2018) for the case of surface

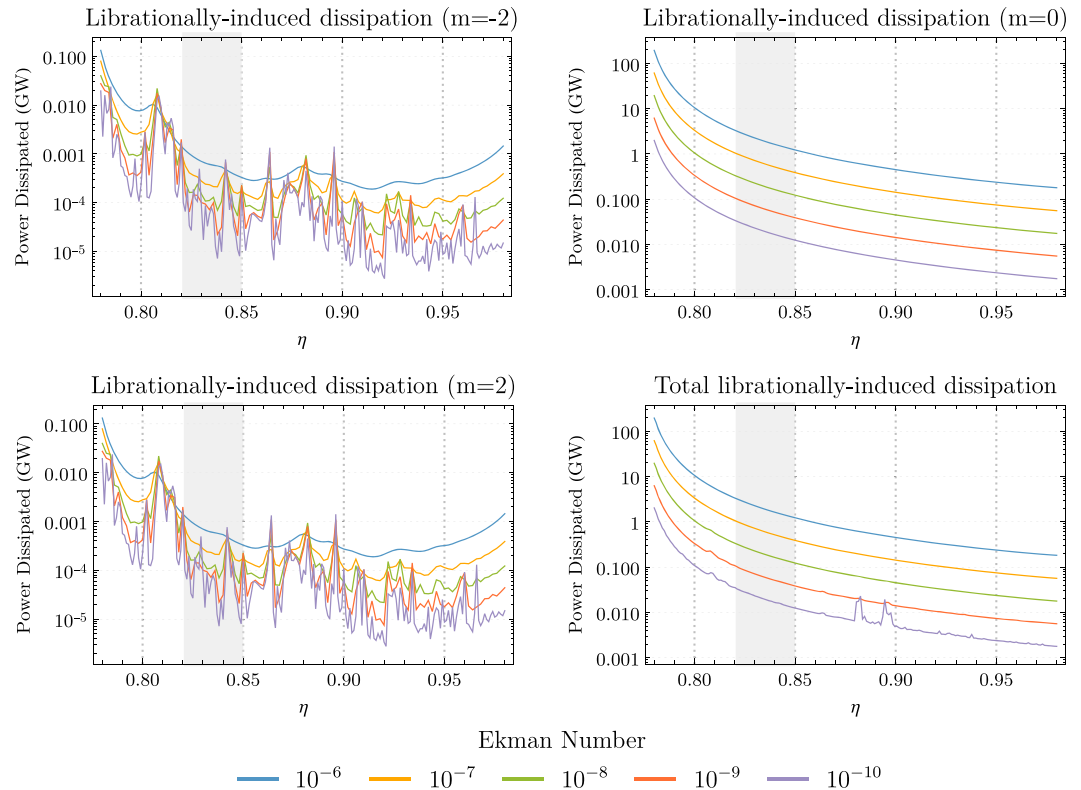


Figure 4. Libration — Viscous dissipation in Enceladus's ocean as a function of η , the aspect ratio of the spherical shell, for different values of the Ekman number. The bottom-right plot is the sum of all the others. The shaded area represents the range $0.82 \leq \eta \leq 0.85$ predicted by models of isostasy.

gravity waves. The principal contribution to the total dissipation comes from the prograde tide ($m = -2$) as expected considering it is the dominant contribution to the tidal potential. The total contribution from the eccentricity tides lies somewhere in the range $10^{-6} < D_{\text{visc}} < 10^{-3}$ GW depending on the presence or absence of a peak.

The peaks in the dissipation profile are due to the augmented contribution caused by the internal shear layers inside the ocean. This can be observed from the two upper plots of Figure 3, which show the density of kinetic energy for two different values of η (both within the range $0.82 < \eta < 0.85$ obtained by Beuthe et al., 2016), one associated to larger dissipation and one to smaller dissipation. The corresponding values of D_{visc} can be read from the bottom plot of Figure 3 and differ by 3 orders of magnitude. The pattern of internal shear layers appears much sharper on the upper-right plot, corresponding to the higher dissipation while they have a lower intensity and seem to fade out more quickly on the upper-left plot.

From the bottom-right plot of Figure 2, we see that the total dissipation caused by tides globally decreases with the Ekman number except for some values of η where resonances can occur. The peaks become sharper as the Ekman number decreases to approach its value for Enceladus ($\text{Ek} = 3.5 \times 10^{-13}$), but the total dissipation remains of the same orders of magnitude. We come back to the interpretation of these resonances in terms of inertial modes in section 4.2.

3.2. Libration

Figure 4 shows the dissipation for $m \in \{-2, 0, 2\}$ and the total dissipation for all these contributions (lower-right panel). We observe the same trend toward larger dissipation for decreasing η , similar to the situation with eccentricity tides.

The contributions $m = 2$ and $m = -2$ lead to identical dissipation profiles, as expected given the symmetrical nature of the forcing. The contribution $m = 0$ dominates for larger values of the viscosity but decreases rapidly as Ek goes down. This is the only contribution that shows no trace of peaks in its profile which indicates that most of the dissipation takes place inside the Ekman boundary layer. This picture is comforted

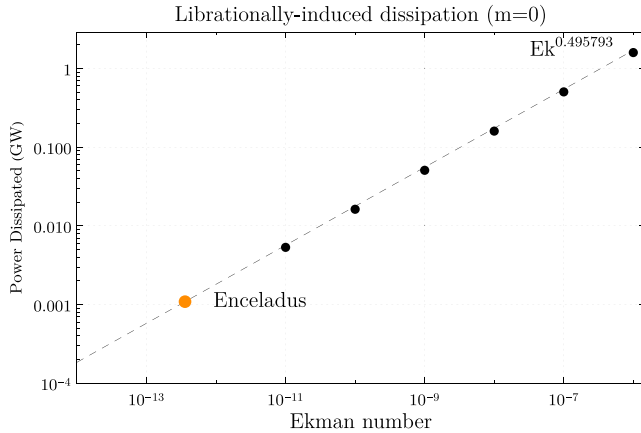


Figure 5. Libration — Viscous dissipation in Enceladus's ocean ($\eta = 0.838$). The behavior $\sim Ek^{1/2}$ (dashed curve) indicates that most of the dissipation takes place inside the Ekman boundary layer by toroidal drag ($m = 0$). This is not true of other components ($m = \pm 2$, see Figure 4). The orange dot indicates the dissipation extrapolated to Enceladus's viscosity. This is the leading source of dissipation inside the moon's ocean.

by noting that the dissipation decreases with decreasing viscosity as $D_{\text{visc}} \sim Ek^{1/2}$, as shown in Figure 5 for $\eta = 0.838$, a scaling law typical of Ekman boundary layers. Extrapolation of this curve to $Ek = 3.5 \times 10^{-13}$ gives $D_{\text{visc}} \sim 0.001$ GW for Enceladus. This is the dominant source of dissipation in the moon's ocean if one disregards the other, more erratic, contributions. The total dissipation due to libration (Figure 4, lower-right panel) also shows how the three components may become commensurable at low Ekman number ($Ek \leq 10^{-10}$) at values of η where there is a peak.

4. Discussion

4.1. Libration as the Dominant Source of Dissipation

Toroidal libration ($m = 0$) dominates over all other sources of dissipation for $Ek > 10^{-10}$, as can be seen on Figures 2 and 4, and becomes commensurable to the other components of libration for lower viscosities. Since the amount of dissipation induced by the toroidal drag scales nicely with the Ekman number, we can extrapolate the amount of dissipation to the Ekman number relevant to Enceladus from Figure 5. The power scales as $\sim Ek^{1/2}$, which indicates the predominant role of the Ekman boundary layer. Extrapolating this power law to $Ek = 3.5 \times 10^{-13}$, the relevant value for Enceladus, we predict a value of 10^{-3} GW for the total dissipation. That is about 4 orders of magnitude below the ~ 10 GW observed by Cassini.

4.2. The Role of Inertial Modes

Our results have revealed how the presence of internal shear layers can lead to a significant increase of the internal dissipation. Previous authors have tried to explain resonances in terms of wave attractors and the critical latitude singularity (Ogilvie, 2013; Rieutord et al., 2000; Rovira-Navarro et al., 2019). We would like to complement this picture with our own interpretation based on the spectrum of free inertial modes.

In the absence of external body force, inertial modes are solutions to

$$\lambda \mathbf{u} + 2\hat{\Omega} \times \mathbf{u} + \nabla p - Ek \nabla^2 \mathbf{u} = 0, \quad (25)$$

which is analogous to equation (19), except that λ now denotes the *complex* eigenvalue. It is sensible to assume that the response to a body force (per unit volume), \mathbf{f} , of frequency ω can be decomposed, at least partially, onto the (infinite) set of inertial modes $\{\mathbf{u}_\alpha\}$:

$$\mathbf{v} \sim \sum_{\alpha} \frac{\langle \mathbf{f} | \mathbf{u}_\alpha \rangle}{|\lambda_\alpha - i\omega|} \mathbf{u}_\alpha, \quad (26)$$

where $\langle \cdot | \cdot \rangle$ denotes the projection operator over pairs of vector fields. Ivers et al. (2014) and Backus and Rieutord (2017) have demonstrated the completeness of the above modal expansion for an inviscid fluid inside a spherical or ellipsoidal container (with no inner core). In analogy with those works, we define the projection operator as $\langle \mathbf{v} | \mathbf{w} \rangle \equiv \text{Re} \int_V \mathbf{v}^* \cdot \mathbf{w}$. A resonance takes place when the factor multiplying one or more \mathbf{u}_α becomes large, which occurs when the distance between the forcing frequency and the eigenvalue approaches zero and/or $\langle \mathbf{f} | \mathbf{u}_\alpha \rangle$ is large. This typically happens when the spatial structure of the forcing shares some similarity with an eigenmode. This formalism can be applied to our case after we have found the relevant body force, \mathbf{f} . Details on how to do so are explained in Appendix B.

Figure 6 illustrates the resonance with inertial waves. The upper and middle panels represent the evolution of the spectrum around $\lambda = i$ (the diurnal frequency, $\omega = 1$, in our set of units) as a function of η for $Ek = 10^{-7}$. The color scale is inherited from the middle plot with lighter colors corresponding to a stronger damping. The lower panel shows a superposition of the dissipation profile (in black) on top of the combination $\frac{\langle \mathbf{f} | \mathbf{u}_\alpha \rangle}{|\lambda_\alpha - i|}$. There is a clear correlation between the two; the peaks in dissipation profile appear where the resonances with the eigenmodes are the strongest.

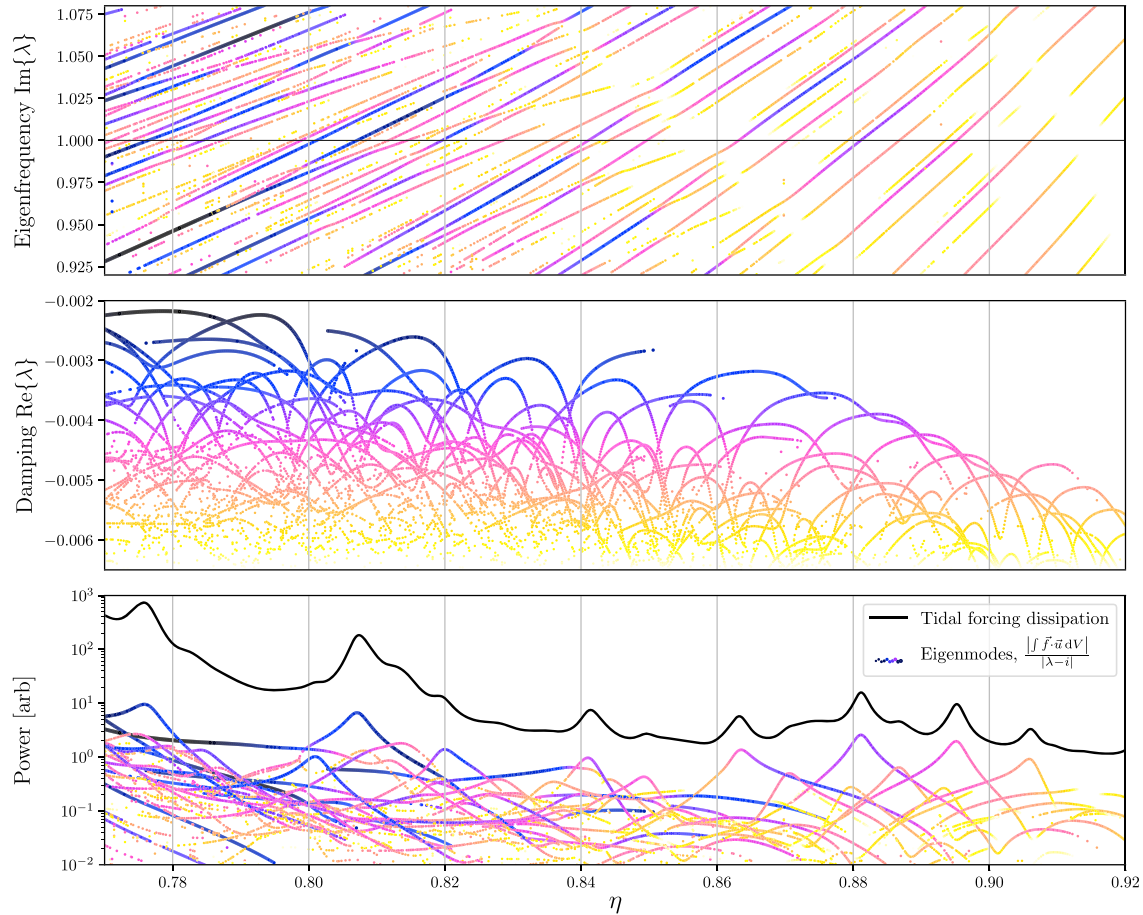


Figure 6. Eccentricity tides — The upper and middle panels represent the imaginary part (frequency) and real part (damping) of the spectrum of eigenvalues of the linear Navier-Stokes equation, respectively. The black curve of the lower panel represents the dissipated power (in arbitrary units). The color curves on that same plot represent the projections of the tidal body force (f) onto the eigenvectors (u) divided by the distance between the unit forcing frequency and the eigenvalue (λ). The color scale is inherited from the middle panel with lighter colors corresponding to a stronger damping ($m = 2$, $\text{Ek} = 10^{-7}$).

4.3. Conclusion and Future Work

We have computed the viscous dissipation in Enceladus's ocean, and we have shown that the combined effect of eccentricity tides and libration is not sufficient to explain the heat flux observed by Cassini. We therefore confirm that the results of Matsuyama et al. (2018) remain valid even when the dissipation of the internal shear layers in the ocean's bulk is taken into account. We show that librationaly induced dissipation dominates tidally induced dissipation, but the overall power dissipated in the ocean is still negligible, as in Rovira-Navarro et al. (2019).

In light of our results, it is clear that the heat flux observed on Enceladus cannot be explained solely by viscous dissipation in the ocean alone, at least at the linear level. The source of heat must therefore be sought elsewhere. The ohmic dissipation in the shear layers due to the presence of Saturn's magnetic field appears as a relevant candidate at first glance. However, the external magnetic field at Enceladus is quite small, of the order $\sim 0.6 \mu\text{T}$, which corresponds to a *Lehnert number* of $\text{Le} \sim 1.6 \times 10^{-6}$. Lin and Ogilvie (2018) have shown that ohmic dissipation dominates over viscous dissipation only when $\text{Le} > \text{Ek}_m^{2/3}$, where Ek_m is the *magnetic Ekman number* which are, respectively, defined as

$$\text{Le} = \frac{B_0}{\Omega R_o \sqrt{\mu \rho}}, \quad \text{Ek}_m = \frac{\nu_m}{\Omega R_o^2}, \quad (27)$$

where B_0 is the background magnetic field, μ is the magnetic permeability, and ν_m is the magnetic diffusivity. Recent estimates of the electrical conductivity inside the ocean (Vance et al., 2018) give $\text{Ek}_m \sim 1$. The ohmic dissipation is therefore unlikely to contribute significantly to the total.

Wilson and Kerswell (2018) have argued that libration could potentially generate turbulence inside the ocean and thus significantly increase the amount of dissipation. Another possibility is that the present heat production does not balance the present heat flow but was larger in the past during periods of larger eccentricities (Ojakangas & Stevenson, 1986).

The observed North-South dichotomy of the moon's surface poses another important puzzle. The southern hemisphere is young and resurfaced, while the northern hemisphere is old and cratered. This problem cannot be addressed in our simplified spherical model. The observed J_3 implies that the icy crust is thinner over the south polar terrain (Iess et al., 2014). We also know that the density of kinetic energy inside the shear layers is higher at the poles, close to the axis of rotation (Rieutord & Valdettaro, 1997), something that is visible on Figure 3. It would be interesting to see how the dissipation at both poles changes when one takes the topography of the crust into account. On the one hand, the internal shear layers tend to be more concentrated toward the poles in the thin ocean limit. On the other hand, our results all indicate a higher value of the dissipation for a thicker ocean. Both regimes are illustrated on the left and right sides of every dissipation profile in the present paper (e.g., Figures 2 and 4).

Appendix A: Tidal and Libration Forcings

A1. Tidal Displacements

We now explain how we compute the tidal displacement using equations (3) and (4).

There are many ways to do so. We base our solution on the representation of the displacement field \mathbf{s} in terms of scalar potentials in analogy with equation (24). Due to the irrotational nature of the forcing, the displacement has no toroidal part so that one can write

$$\mathbf{s} = \nabla \times \nabla \times (\mathcal{P} \mathbf{r}). \quad (\text{A1})$$

Using the above, we can arrive at an independent equation in terms of the spherical harmonics components of \mathcal{P} after taking the curl of equation (4) twice. The term proportional to ω in equation (4) can be safely omitted in the solid layers, which greatly simplifies the analytical treatment. We illustrate the validity of this approximation below by comparing the analytical solution to the result of a direct numerical integration in which all the terms of equation (4) are retained. The equation for the $\mathcal{P}_{\ell,m}$ reduces to

$$\mathcal{P}_{\ell,m}'' + \frac{2}{r} \mathcal{P}_{\ell,m}' - \frac{\ell(\ell+1)}{r^2} \mathcal{P}_{\ell,m} = 0, \quad (\text{A2})$$

in the ocean and

$$\mathcal{P}_{\ell,m}'''' + \frac{4}{r} \mathcal{P}_{\ell,m}''' - \frac{2\ell(\ell+1)}{r^2} \mathcal{P}_{\ell,m}'' + \frac{\ell(\ell+1)(\ell-1)(\ell+2)}{r^4} \mathcal{P}_{\ell,m} = 0, \quad (\text{A3})$$

in the solid parts (a prime denotes the radial derivative). These correspond to the spherical harmonics coefficients of the Laplacian and bi-Laplacian of \mathcal{P} . The spherical harmonics components of equation (3) are

$$\delta\phi_{\ell,m}'' + \frac{2}{r} \delta\phi_{\ell,m}' - \frac{\ell(\ell+1)}{r^2} \delta\phi_{\ell,m} = 0, \quad (\text{A4})$$

which is valid everywhere. From the above, we see that the general solution for $\delta\phi_{\ell,m}$ and $\mathcal{P}_{\ell,m}$ involve six integration constants in each solid layer and four in the ocean. The value of these must be determined from the junction conditions (equations (6) to (9)) together with the components of the tidal potential (equations (11) to (13)).

Figure A1 shows the amplitude of the radial and tangential displacements at the top and bottom of the ocean for a unit forcing. The curves represent the analytical solutions obtained using the simplifying procedure described above where we neglect the terms of equation (4) proportional to ω in the solid layers. The markers are the results of direct numerical integration of the equation of section 2.1.2 for a few selected values of η . The good agreement between the analytical and numerical solutions illustrates the validity of our analytical treatment.

The analytical expressions for the displacement are quite long and impractical to manipulate. Instead, we provide a set of simplified expressions based on Padé approximants on the interval $\eta \in [\frac{16}{21}, 1]$. The number

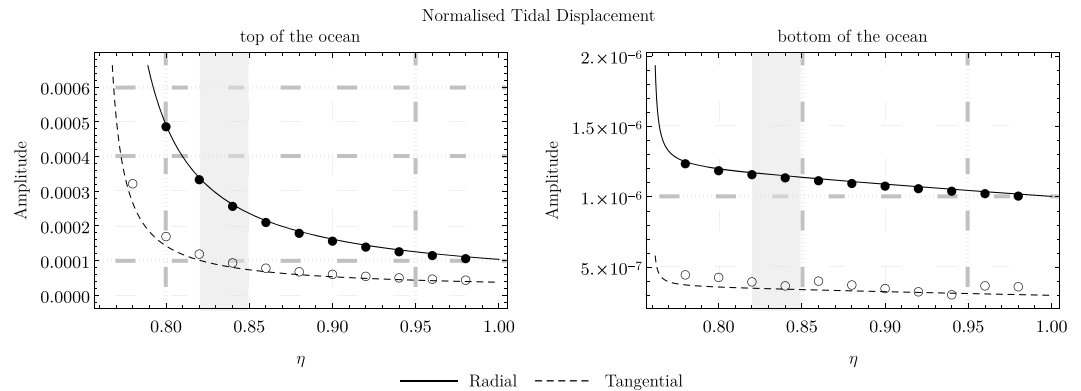


Figure A1. Tidal displacement at the top and bottom of the ocean as a function of the aspect ratio, η , and normalized with the tidal potential. The corresponding analytical expressions are given in equations (A6) to (A8). The curves corresponds to the result of the analytical solution outlined in section A1. The markers results from the direct numerical integration of the equations of section 2.1.2. The shaded area represents the range $0.82 \leq \eta \leq 0.85$ predicted by models of isostasy.

³⁷₄₂ that appears in the following expressions is the average value of η on the interval $[\frac{16}{21}, 1]$. These expressions give the tidal displacement for a unit forcing. One recovers the three components of the actual displacement (in units of the ocean's radius), after multiplication by equations (11), (12), or (13):

Radial displacements (normalized)

$$\text{top} \rightarrow \frac{(7.40517 \times 10^{-4}) \left(\eta - \frac{37}{42} \right)^3 + (6.59337 \times 10^{-4}) \left(\eta - \frac{37}{42} \right)^2 + (2.7655 \times 10^{-4}) \left(\eta - \frac{37}{42} \right) + 5.69317 \times 10^{-5}}{59.0717 \left(\eta - \frac{37}{42} \right)^3 + 26.5663 \left(\eta - \frac{37}{42} \right)^2 + 10.3018 \left(\eta - \frac{37}{42} \right) + 0.961236} \quad (\text{A5})$$

$$\text{bottom} \rightarrow \frac{(-8.42775 \times 10^{-9}) \left(\eta - \frac{37}{42}\right)^3 + (1.88871 \times 10^{-5}) \left(\eta - \frac{37}{42}\right)^2 + (1.14009 \times 10^{-5}) \left(\eta - \frac{37}{42}\right) + 1.1095 \times 10^{-6}}{17.7942 \left(\eta - \frac{37}{42}\right)^3 + 25.8487 \left(\eta - \frac{37}{42}\right)^2 + 11.1432 \left(\eta - \frac{37}{42}\right) + 1.00059} \quad (\text{A6})$$

Tangential displacements (normalized)

$$\text{top} \rightarrow \frac{(1.23779 \times 10^{-3}) \left(\eta - \frac{37}{42} \right)^3 + (1.19261 \times 10^{-3}) \left(\eta - \frac{37}{42} \right)^2 + (5.91035 \times 10^{-4}) \left(\eta - \frac{37}{42} \right) + 1.79239 \times 10^{-4}}{49.5224 \left(\eta - \frac{37}{42} \right)^3 + 22.7936 \left(\eta - \frac{37}{42} \right)^2 + 10.1381 \left(\eta - \frac{37}{42} \right) + 0.979681} \quad (\text{A7})$$

$$\text{bottom} \rightarrow \frac{(-2.52832 \times 10^{-9}) \left(\eta - \frac{37}{42} \right)^3 + (5.66613 \times 10^{-6}) \left(\eta - \frac{37}{42} \right)^2 + (3.42027 \times 10^{-6}) \left(\eta - \frac{37}{42} \right) + 3.32849 \times 10^{-7}}{17.7942 \left(\eta - \frac{37}{42} \right)^3 + 25.8487 \left(\eta - \frac{37}{42} \right)^2 + 11.1432 \left(\eta - \frac{37}{42} \right) + 1.00059} \quad (\text{A8})$$

A2. Libration Forcing

The value of the parameters α_2 and ϵR which appear in equation (18), at the top and bottom of the ocean are represented on Figure A2. These result from the analytical resolution of the libration model presented in Van Hoolst et al. (2016). The analytical expressions for the amplitude ϵR are quite long and impractical, so we provide an approximation on the interval $\eta \in [\frac{16}{21}, 1]$ based on Padé approximants (all expressions are in dimensionless units):

Amplitude at the top and bottom of the ocean

$$\text{top} \rightarrow e R = \frac{0.0142482 \left(\eta - \frac{37}{42} \right)^4 + 0.0234122 \left(\eta - \frac{37}{42} \right)^3 + 0.0177355 \left(\eta - \frac{37}{42} \right)^2 + 0.00669395 \left(\eta - \frac{37}{42} \right) + 0.00113254}{25.2386 \left(\eta - \frac{37}{42} \right)^4 + 45.0416 \left(\eta - \frac{37}{42} \right)^3 + 33.2167 \left(\eta - \frac{37}{42} \right)^2 + 12.0145 \left(\eta - \frac{37}{42} \right) + 0.957481}, \quad (\text{A9})$$

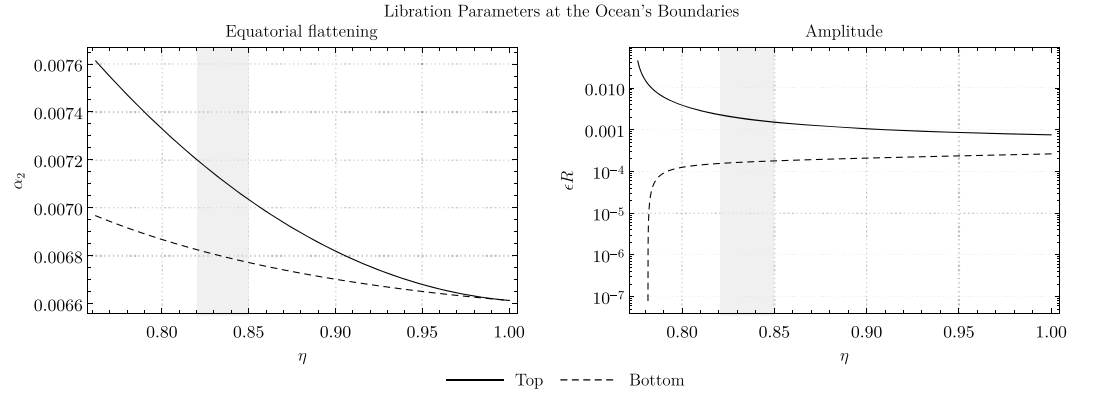


Figure A2. Equatorial flattening (left panel) and amplitude of libration (right panel) at the top and bottom of the ocean (see equation (18)). The corresponding analytical expressions for the amplitude are given in equations (A9) to (A10). The shaded area represents the range $0.82 \leq \eta \leq 0.85$ predicted by models of isostasy. R denotes the radius at the top and bottom of the ocean depending on the curve that is considered.

bottom $\rightarrow \epsilon R$

$$= \frac{0.00177273 \left(\eta - \frac{37}{42} \right)^4 + 0.00779929 \left(\eta - \frac{37}{42} \right)^3 + 0.00780726 \left(\eta - \frac{37}{42} \right)^2 + 0.00272733 \left(\eta - \frac{37}{42} \right) + 0.000201493}{0.997077 \left(\eta - \frac{37}{42} \right)^4 - 4.0871 \left(\eta - \frac{37}{42} \right)^3 + 11.8146 \left(\eta - \frac{37}{42} \right)^2 + 10.7977 \left(\eta - \frac{37}{42} \right) + 1.01542} \quad (\text{A10})$$

Appendix B: Tidal Dissipation With a Body Force

Some authors (Ogilvie, 2013; Rieutord et al., 2000; Rovira-Navarro et al., 2019) presented a slightly different formalism to compute the dissipation caused by tides. We now want to show the equivalence to ours. Their approach is based on the decomposition of the velocity field in two parts:

$$\mathbf{v} = \mathbf{v}^{(\text{eq})} + \mathbf{v}^{(d)}. \quad (\text{B1})$$

The first part is attributed to the displacement caused by the equilibrium tides. Plugging the above ansatz into the momentum equation, leads to an equation for $\mathbf{v}^{(d)}$:

$$i\omega \mathbf{v}^{(d)} + 2\hat{\Omega} \times \mathbf{v}^{(d)} + \nabla p - \text{Ek} \nabla^2 \mathbf{v}^{(d)} = \mathbf{f}, \quad (\text{B2})$$

where $\mathbf{f} = -i\omega \mathbf{v}^{(\text{eq})} - 2\hat{\Omega} \times \mathbf{v}^{(\text{eq})}$ is treated as a body force per unit volume. Ogilvie (2013) argues that when $\mathbf{v}^{(\text{eq})}$ is computed from the theory of equilibrium tides, one has $\mathbf{v}^{(\text{eq})} = \nabla X$, where X is a harmonic scalar function ($\nabla^2 X = 0$, owing to the condition of incompressibility). The harmonic component of degree ℓ therefore reads $X_{\ell,m} = (A_{\ell,m} r^\ell + \frac{B_{\ell,m}}{r^{\ell+1}})$, where $A_{\ell,m}$ and $B_{\ell,m}$ are scalar constants that depend on the deformation (see Ogilvie, 2013, for details).

In our approach, we do not decompose the velocity field explicitly and rather solve for the full momentum equation, including the potential perturbation. This extra term, however, can be merged with the reduced pressure, which, in turn, disappears completely when one solves for the vorticity in the volume. The effect of the potential thus appears only in the expression of the boundary condition. This is the reason for which the condition of continuity of the total flow, \mathbf{v} , across the physical boundaries is given by our equation (23) while Rovira-Navarro et al. (2019) simply have $\mathbf{v}^{(d)} = 0$.

The two methods lead to results that are completely equivalent. The approach based on the boundary forcing is perhaps conceptually simpler and better suited to the usual language of fluid dynamicists. The description based on the body force \mathbf{f} , on the other hand, has the advantage to be directly usable in the discussion presented in section 4.2.

Figure B1 is a reproduction of figure 6(b) in Rovira-Navarro et al. (2019) using our settings. The discrepancy between the predicted amounts of dissipation in the deep ocean limit (left part of our plot and right part

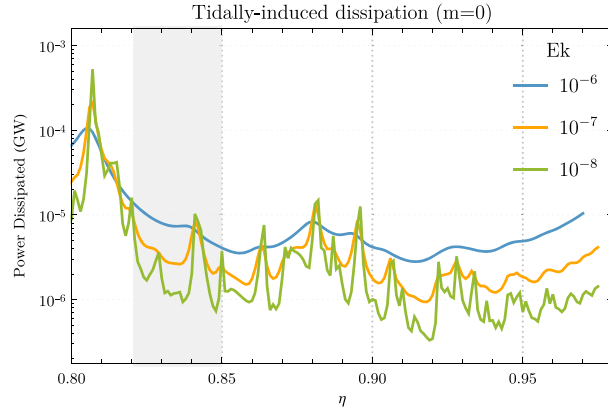


Figure B1. Eccentricity tides — Detailed version of the upper-right panel of Figure 2 for comparison with Rovira-Navarro et al. (2019, see their fig. 6(b)).

of theirs) is due to the presence of an icy crust in our model, while it is neglected in their study. This leads to a decrease in the amount of energy dissipated in agreement with the results of Matsuyama et al. (2018). Our curves also go up slightly in the thin ocean limit on the right part of the plot. This feature is absent in Rovira-Navarro et al. (2019) and is likely due to the fact that they use a purely radial forcing, thus neglecting tangential displacement at the boundary. When we take these into account, resonances appear in the thin ocean limit consistently with the results of Ogilvie (2009). Apart from these differences, our curves bear a striking resemblance with theirs, which illustrates the equivalence of our approaches.

Appendix C: Navier-Stokes Equation in Spherical Harmonics

Here, below, we provide the expressions used to compute the flow inside the ocean. These are based on the curl of equation (19), that is, the equation of vorticity, and the parametrization equation (24).

$$\begin{aligned}
 r^4(\hat{\mathbf{r}} \cdot \nabla \times \nabla \times \text{Equation (19)}) &\Rightarrow ir^2(\omega\ell(\ell+1) - 2m) \left[\ell(\ell+1)\mathcal{P}_{\ell,m} - 2r\mathcal{P}'_{\ell,m} - r^2\mathcal{P}''_{\ell,m} \right] \\
 &+ \frac{2r^3(\ell-1)^2(\ell+1)\sqrt{(\ell-m)(m+\ell)}}{2\ell-1} \mathcal{T}_{\ell-1,m} \\
 &- \frac{2r^3\ell(\ell+2)^2\sqrt{(-m+\ell+1)(m+\ell+1)}}{2\ell+3} \mathcal{T}_{\ell+1,m} \\
 &- \frac{2r^4(\ell^2-1)\sqrt{(\ell-m)(m+\ell)}}{2\ell-1} \mathcal{T}'_{\ell-1,m} \\
 &- \frac{2r^4\ell(\ell+2)\sqrt{(-m+\ell+1)(m+\ell+1)}}{2\ell+3} \mathcal{T}'_{\ell+1,m} \\
 &+ Ek \quad \ell(\ell+1) \left[(\ell-1)\ell(\ell+1)(\ell+2)\mathcal{P}_{\ell,m} \right. \\
 &\quad \left. - 2r^2\ell(\ell+1)\mathcal{P}''_{\ell,m} + 4r^3\mathcal{P}'''_{\ell,m} + r^4\mathcal{P}''''_{\ell,m} \right] = 0,
 \end{aligned} \tag{C1}$$

$$\begin{aligned}
 -r^2(\hat{\mathbf{r}} \cdot \nabla \times \text{Equation (19)}) &\Rightarrow ir^2(\omega\ell(\ell+1) - 2m) \mathcal{T}_{\ell,m} \\
 &+ \frac{2r(\ell-1)^2(\ell+1)\sqrt{(\ell-m)(m+\ell)}}{2\ell-1} \mathcal{P}_{\ell-1,m} \\
 &- \frac{2r\ell(\ell+2)^2\sqrt{(-m+\ell+1)(m+\ell+1)}}{2\ell+3} \mathcal{P}_{\ell+1,m} \\
 &- \frac{2r^2(\ell^2-1)\sqrt{(\ell-m)(m+\ell)}}{2\ell-1} \mathcal{P}'_{\ell-1,m} \\
 &- \frac{2r^2\ell(\ell+2)\sqrt{(-m+\ell+1)(m+\ell+1)}}{2\ell+3} \mathcal{P}'_{\ell+1,m} \\
 &+ Ek \quad \ell(\ell+1) \left[\ell(\ell+1)\mathcal{T}_{\ell,m} - 2r\mathcal{T}'_{\ell,m} - r^2\mathcal{T}''_{\ell,m} \right] = 0,
 \end{aligned} \tag{C2}$$

where a prime denotes a radial derivative.

Acknowledgments

We would like to thank Marc Rovira-Navarro and the anonymous reviewer whose comments helped us to significantly improved the quality of our manuscript. The research leading to these results has received funding from the European Research Council (ERC) under the European Union's Horizon 2020 research and innovation programme (Advanced Grant Agreement 670874). The work presented here is fully computational. All the relevant information needed to reproduce our results is in the method and the appendices of this manuscript. Our results based on the resolution of the Navier-Stokes equation were obtained using the code *Tintin* developed by the authors and available online (<https://bitbucket.org/repepo/tintin>). The formal release of this code will be the subject of a future publication.

References

- Běhouňková, M., Souček, O., Hron, J., & Čadek, O. (2017). Plume activity and tidal deformation on Enceladus influenced by faults and variable ice shell thickness. *Astrobiology*, 17(9), 941–954.
- Běhouňková, M., Tobie, G., Choblet, G., & Čadek, O. (2010). Coupling mantle convection and tidal dissipation: Applications to Enceladus and Earth-like planets. *Journal of Geophysical Research*, 115, E09011. <https://doi.org/10.1029/2009JE003564>
- Backus, G. (1986). Poloidal and toroidal fields in geomagnetic field modeling. *Reviews of Geophysics*, 24(1), 75–109.
- Backus, G., & Rieutord, M. (2017). Completeness of inertial modes of an incompressible inviscid fluid in a corotating ellipsoid. *Physical Review E*, 95(5), 1–16.
- Baland, R. M., & Van Hoolst, T. (2010). Librations of the Galilean satellites: The influence of global internal liquid layers. *Icarus*, 209(2), 651–664.
- Baland, R. M., Yseboodt, M., & Van Hoolst, T. (2016). The obliquity of Enceladus. *Icarus*, 268, 12–31.
- Barr, A. C., & McKinnon, W. B. (2007). Convection in Enceladus' ice shell: Conditions for initiation. *Geophysical Research Letters*, 34, L09202. <https://doi.org/10.1029/2006GL028799>
- Beuthe, M., Rivoldini, A., & Trinh, A. (2016). Enceladus's and Dione's floating ice shells supported by minimum stress isostasy. *Geophysical Research Letters*, 43, 10,088–10,096. <https://doi.org/10.1002/2016GL070650>
- Čadek, O., Tobie, G., Van Hoolst, T., Massé, M., Choblet, G., Lefèvre, A., et al. (2016). Enceladus's internal ocean and ice shell constrained from Cassini gravity, shape, and libration data.
- Chen, E. M. A., & Nimmo, F. (2011). Obliquity tides do not significantly heat Enceladus. *Icarus*, 214(2), 779–781.
- Choblet, G., Tobie, G., Sotin, C., Běhouňková, M., Čadek, O., Postberg, F., & Souček, O. (2017). Powering prolonged hydrothermal activity inside Enceladus. *Nature Astronomy*, 1(12), 841–847.
- Dahlen, F. A., & Tromp, J. (1998). *Theoretical global seismology*. Princeton, NJ: Princeton University Press.
- Greenspan, H. P. (1968). *The theory of rotating fluids*, Cambridge Monographs on Mechanics. Cambridge: Cambridge University Press.
- Hay, H. C., & Matsuyama, I. (2017). Numerically modelling tidal dissipation with bottom drag in the oceans of Titan and Enceladus. *Icarus*, 281, 342–356.
- Hay, H. C., & Matsuyama, I. (2019). Nonlinear tidal dissipation in the subsurface oceans of Enceladus and other icy satellites. *Icarus*, 319, 68–85.
- Hemingway, D. J., & Mittal, T. (2019). Enceladus's ice shell structure as a window on internal heat production. *Icarus*, 332, 111–131.
- Howett, C. J. A., Spencer, J. R., Pearl, J., & Segura, M. (2011). High heat flow from Enceladus' south polar region measured using 10–600 cm⁻¹ Cassini/CIRS data. *Journal of Geophysical Research*, 116, E03003. <https://doi.org/10.1029/2010JE003718>
- Iess, L., Stevenson, D. J., Parisi, M., Hemingway, D., Jacobson, R. A., Lunine, J. I., et al. (2014). The gravity field and interior structure of Enceladus. *Science*, 344, 78–80.
- Ivers, D. J. J., Jackson, A., & Winch, D. (2014). Enumeration, orthogonality and completeness of the incompressible coriolis modes in a sphere. *Journal of Fluid Mechanics*, 468–498.
- Landau, L. D., & Lifshitz, E. M. (1987). *Course of theoretical physics, vol. 6: Fluid mechanics 2nd ed.* Oxford: Pergamon Press.
- Lin, Y., & Ogilvie, G. I. (2018). Tidal dissipation in rotating fluid bodies: The presence of a magnetic field. *Monthly Notices of the Royal Astronomical Society*, 474(2), 1644–1656.
- Love, A. E. H. (1909). The yielding of the Earth to disturbing forces. *Nature*, 80, 252–253.
- Matsuyama, I., Beuthe, M., Hay, H. C., Nimmo, F., & Kamata, S. (2018). Ocean tidal heating in icy satellites with solid shells. *Icarus*, 312, 208–230.
- Morize, C., Le Bars, M., Le Gal, P., & Tilgner, A. (2010). Experimental determination of zonal winds driven by tides. *Physical Review Letters*, 104(21), 28–31.
- Nimmo, F., Barr, A. C., Běhouňková, M., & McKinnon, W. B. (2018). The thermal and orbital evolution of Enceladus: Observational constraints and models. *Enceladus and the Icy Moons of Saturn*, 475, 79–94.
- Ogilvie, G. I. (2009). Tidal dissipation in rotating fluid bodies: A simplified model. *Monthly Notices of the Royal Astronomical Society*, 396(2), 794–806.
- Ogilvie, G. I. (2013). Tides in rotating barotropic fluid bodies: The contribution of inertial waves and the role of internal structure. *Monthly Notices of the Royal Astronomical Society*, 429(1), 613–632.
- Ojakangas, G. W., & Stevenson, D. J. (1986). Episodic volcanism of tidally heated satellites with application to Io. *Icarus*, 66(2), 341–358.
- Poincaré, H. (1885). Sur l'équilibre d'une masse fluide animée d'un mouvement de rotation. *Acta Mathematica*, 7(1), 259–380.
- Porco, C. C., Helfenstein, P., Thomas, P. C., Ingersoll, A. P., Wisdom, J., West, R., et al. (2006). Cassini observes the active south pole of Enceladus. *Science*, 311, 1393–1401.
- Rekier, J., Trinh, A., Triana, S. A., & Dehant, V. (2018). Inertial modes in near-spherical geometries. *Geophysical Journal International*, 216, 777–793.
- Rieutord, M., Georgeot, B., & Valdetarro, L. (2000). Inertial waves in a rotating spherical shell: Attractors and asymptotic spectrum. *Journal of Fluid Mechanics*, 435, 42.
- Rieutord, M., & Valdetarro, L. (1997). Inertial waves in a rotating spherical shell. *Journal of Fluid Mechanics*, 341, 77–99.
- Roberts, J. H. (2015). The fluffy core of Enceladus. *Icarus*, 258, 54–66.
- Rovira-Navarro, M., Rieutord, M., Gerkema, T., Maas, L. R. M., vander Wal, W., & Vermeersen, B. (2019). Do tidally-generated inertial waves heat the subsurface oceans of Europa and Enceladus? *Icarus*, 321, 126–140. <https://doi.org/10.1016/j.icarus.2018.11.010>
- Spencer, J. R., Pearl, J. C., Segura, M., Flasar, F. M., Mamoutkine, A., Romani, P., et al. (2006). Cassini encounters Enceladus: Background and the discovery of a south polar hot spot. *Science*, 311, 1401–1405.
- Thomas, P. C., Tajeddine, R., Tiscareno, M. S., Burns, J. A., Joseph, J., Lored, T. J., et al. (2016). Enceladus's measured physical libration requires a global subsurface ocean. *Icarus*, 264, 37–47.
- Triana, S. A., Rekier, J., Trinh, A., & Dehant, V. (2019). The coupling between inertial and rotational eigenmodes in planets with liquid cores. *Geophysical Journal International*, 218, 1071–1086. <https://doi.org/10.1093/gji/ggz212>
- Tyler, R. H. (2009). Ocean tides heat enceladus. *Geophysical Research Letters*, 36, L15205. <https://doi.org/10.1029/2009GL038300>
- Tyler, R. (2014). Comparative estimates of the heat generated by ocean tides on icy satellites in the outer solar system. *Icarus*, 243, 358–385.
- Van Hoolst, T., Baland, R. M., & Trinh, A. (2016). The diurnal libration and interior structure of Enceladus. *Icarus*, 277, 311–318.
- Vance, S. D., Panning, M. P., Stähler, S., Cammarano, F., Bills, B. G., Tobie, G., et al. (2018). Geophysical investigations of habitability in ice-covered ocean worlds. *Journal of Geophysical Research: Planets*, 123, 180–205. <https://doi.org/10.1002/2017JE005341>
- Wilson, A., & Kerswell, R. R. (2018). Can libration maintain Enceladus's ocean? *Earth and Planetary Science Letters*, 500, 41–46.